Friction

Research Article

Study on the wear performance of TiAl–P/M superalloy friction pairs: An experimental investigation and wear model

Shaomeng Li[1,†], Junqing Tan[1,†], Chao Wang[1], Hongjian Zhang[1,2,3,✉], Haitao Cui[1,2,3]

Cite this article: Li SM, Tan JQ, Wang C, et al. *Friction* 2026, **14**: 9441196. https://doi.org/10.26599/FRICT.2025.9441196

ABSTRACT: In this study, friction and wear tests were conducted on a TiAl alloy and a nickel-based powder metallurgy (P/M) superalloy. The test results were analyzed and compared to elucidate the friction and wear mechanisms of the two materials and to validate the proposed wear model. These findings indicate that high-hardness oxidized composite debris accumulates on the contact surface. In the early stage, ploughing predominates, leading to an accelerated wear rate. As friction progresses, the accumulation of debris and the formation of a hardened layer partially mitigate the wear rate. However, prolonged friction causes fragmentation of the debris layer, and the subsequent interaction between the hardened debris and the surface promotes additional ploughing, thereby increasing the wear rate once more. This study developed an energy-based wear model that accounts for the observed reduction in the coefficient of friction (COF) with increasing normal load and sliding frequency. The discrepancy between the fitted and experimentally measured friction coefficients is within 20%. Simulations based on this model produced wear depth predictions within a 5 μm margin of error relative to experimental measurements, thereby demonstrating high predictive accuracy.

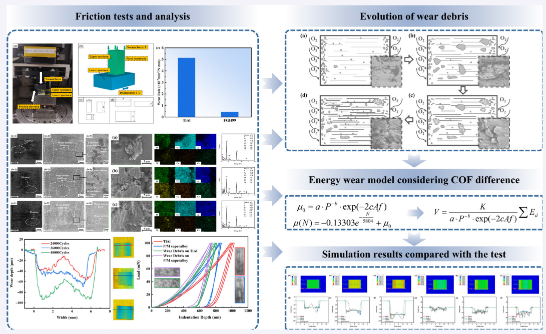

KEYWORDS: TiAl alloy; coefficient of friction (COF); wear model; wear mechanism; wear debris evolution

1 Introduction

In engineering design, accurate quantification of wear is essential for predicting the service life of industrial components. At present, two principal wear-prediction models are widely recognized: the Archard wear model [1] and the frictional-energy model [2–5]. The Archard wear model relates total wear loss to the product of the normal force and fretting sliding distance. During the tribological process, approximately 84%–91% of the input energy is dissipated as heat, whereas 9%–16% is retained in the subsurface of the contact pair as lattice strain energy. When the stored energy density exceeds the material yield threshold, it induces dislocation slip or microcrack initiation, ultimately resulting in material spalling and the generation of wear debris. Mindlin and Deresiewicz [6] conducted pioneering research on the interfacial behavior of elastic-sphere contact systems under combined loading. They reported that microscopic slip, plastic deformation, and energy dissipation mechanisms at the contact interface lead to pronounced path dependence in the traction–displacement relationship. The dynamic response is influenced not only by the initial loading conditions but also by a nonlinear correlation with the instantaneous rate of change in the loading process. Woydt and Mohrbacher [7] demonstrated through energy-decomposition analysis that tangential frictional work is the primary source of interfacial energy dissipation, and the cumulative dissipated frictional energy can be expressed as $E_d = \int_{x_1}^{x_2} F_f \mathrm{d}S$. Li et al. [8] incorporated a temperature-effect correction factor into the traditional energy-based wear model and developed a two-dimensional thermomechanical coupling model for fretting wear prediction. The interactions among the number of cycles, relative motion speed, and cumulative plastic damage of the material were quantitatively analyzed. Jahangiri et al. [9] experimentally verified the linear proportional relationship between cumulative dissipated energy and wear volume $V = \alpha E_d$ and developed a wear prediction model with the energy conversion coefficient α as the core parameter. Yue and Abdel Wahab [10] proposed an innovative energy-based wear model incorporating the dynamic response of the friction coefficient and systematically investigated its time-varying effects on the material removal rate and wear rate. By building an energy-based wear model, Choudhry et al. [11] refined the Archard wear model by introducing a more sophisticated method to determine the wear

† Shaomeng Li and Junqing Tan contributed equally to this work.

[1] College of Energy & Power Engineering, Nanjing University of Aeronautics and Astronautics, Nanjing 210016, China. [2] Aeroengine Thermal Environment and Structure Key Laboratory of Ministry of Industry and Information Technology, Nanjing University of Aeronautics and Astronautics, Nanjing 210016, China. [3] State Key Laboratory of Mechanics and Control for Aerospace Structures, Nanjing University of Aeronautics and Astronautics, Nanjing 210016, China.

✉ Corresponding author. E-mail: zhanghongjian@nuaa.edu.cn

Received: March 11, 2025; Revised: October 30, 2025; Accepted: November 26, 2025

coefficient via deformation energy, thereby enhancing the correlation between wear and the applied load. Liskiewicz et al. [12] introduced the equivalent "miner-energy" wear model, which is capable of estimating the durability of a coating. On the basis of the overall energy–wear approach, the wear depth is expressed as a function of the maximum cumulative dissipated energy density. In summary, the friction-energy wear model not only incorporates the coefficient of friction (COF) but also correlates wear with frictional energy. This approach can be extended to the entire contact interface via the local energy-based wear method. More simulation calculation methods for wear have been investigated [13–15]. However, the wear coefficient is typically assumed to be constant under varying frictional conditions in both models. The stability of the COF under different operating conditions [16, 17] affects the wear coefficient and, consequently, the outcomes of wear simulations. Therefore, it is crucial to develop a more universal friction-and-wear model.

TiAl alloys have emerged as highly competitive lightweight, high-temperature structural materials in the automotive and aerospace industries because of their low density, high specific strength, excellent flame retardancy, superior high-temperature oxidation resistance, and outstanding high-temperature creep resistance [18, 19]. It has broad application prospects in components such as automotive engine exhaust valves and aeroengine turbine blades. To meet the requirements of the new generation of aeroengines, a third-generation powder metallurgy (P/M) superalloy exhibiting high strength, superior damage tolerance, excellent high-temperature resistance, and enhanced durability was developed. P/M superalloys have been extensively employed in the fabrication of aeroengine turbine disks. In aeroengine turbine assemblies, blades supported by TiAl alloy are attached to turbine disks made of P/M superalloys via tenon connections. Owing to centrifugal forces and blade vibrations during engine operation, wear occurs at the contact surfaces of the tenon connections. The generation of wear increases the contact gap, altering the structural vibration characteristics and potentially compromising engine operational safety. Therefore, the friction and wear behavior of TiAl alloy–P/M superalloy friction pairs critically influences the reliability of aeroengine turbine components.

For friction pairs composed of dissimilar materials, material differences result in variations in the contact surface properties, including roughness, coefficient of friction, surface hardness, and residual surface stress. Moreover, dissimilar materials may undergo chemical reactions during friction, and the adhesion of reaction products on the surface can alter the inherent frictional performance. In studies on the friction and wear behavior of dissimilar material pairs, Huttunen-Saarivirta et al. [20] investigated 6082 aluminum alloy–H13 tool steel pairs at both room and elevated temperatures. They reported that oxidation significantly accelerates wear in tool steel and that material loss increases with increasing temperature. Some wear debris generated from the steel plate accumulates on the pin surface, forming a glaze layer capable of plastic deformation. Xu et al. [21] fabricated fixed pins of GS-18NiMoCr36 with varying hardness levels paired with a rotating 42CrMo steel ring to form friction pairs. This experimental setup was employed to investigate the effects of varying hardness combinations on wear performance. The results indicate that the wear weight loss tends to increase–decrease–increase with increasing load. The observed wear mechanisms alternated between oxidative wear and adhesive wear. Furthermore, the degree of wear weight loss decreased with increasing hardness of the fixed pins, suggesting that increasing the hardness within a specific range can markedly improve the wear resistance. Dong et al. [22] investigated the tribological properties of Al_2O_3 ceramic–1Cr18Ni9Ti stainless steel friction pairs in pure water and hydrogen peroxide solutions at various concentrations. Comprehensive analysis revealed that the primary wear mechanisms for the Al_2O_3 ceramic–1Cr18Ni9Ti stainless steel pair in hydrogen peroxide solutions were adhesive wear, abrasive wear, and ploughing wear. Chen et al. [23] investigated the friction and wear behavior of DD6 single-crystal superalloys and GH3536 superalloys at 750 °C between aeroengine turbine blades and edge plate damping blocks. The results indicate that the wear modes of the DD6–GH3536 friction pair include adhesive wear, abrasive wear, and oxidative wear. The primary sources of damage were surface deformation and material transfer at the contact interface. Zhao et al. [24] employed Si_3N_4 balls to study the fretting wear properties of GH4169 before and after laser shock peening (LSP). Compared with the untreated sample, the LSP-treated sample is more prone to plastic deformation rather than material transfer, thereby promoting the transition of the wear mechanism from adhesive wear to abrasive wear. Therefore, the LSP-induced gradient microstructure is considered the primary contributor to the marked enhancement of the high-temperature fretting wear performance of GH4169. Currently, most studies on the friction and wear behavior of dissimilar materials focus on analyzing only one of the constituent materials. Even when the materials of the grinding component and test specimen are interchanged, systematic comparative studies encompassing both materials remain scarce. Therefore, investigating the friction and wear properties of dissimilar TiAl alloy–P/M superalloy materials is crucial for enhancing the operational reliability of turbine disks and blades, as well as improving the accuracy of simulation-based predictions.

This study presents a comparative analysis of the friction and wear behavior of TiAl alloy–P/M superalloy dissimilar-material pairs, aiming to elucidate the fundamental friction and wear mechanisms during sliding interactions. Building upon the observed inverse correlation between the stable COF and increasing normal load and sliding frequency under controlled operating conditions, we developed an energy-based wear model that systematically incorporates COF variations across operational parameters. Systematic validation procedures were subsequently performed to evaluate the reliability of the proposed wear model.

2 Details of the wear model and test

2.1 Test details

Friction and wear tests were conducted on P/M superalloy and TiAl alloy samples. The energy dispersive spectrometer (EDS) results for both materials are presented in Fig. 1. In the P/M superalloy, Ni, Cr, and Co are the predominant elements, with Ni accounting for 39.359%; minor amounts of Ti and Al are also present. In the TiAl alloy, Ti and Al are the major constituents, with Ti and Al accounting for 37.346% and 34.393%, respectively; minor amounts of Nb and Cr are also present. Friction tests were performed via a UMT-2 Universal Mechanical Tester. Friction and wear tests were conducted under reciprocating loading conditions to simulate surface contact. Detailed schematics of the experimental setup are shown in Figs. 2(a) and 2(b). The upper and lower samples are illustrated in Figs. 2(c) and 2(d), with a contact area of 5 mm × 5 mm. The test parameters are summarized in Table 1. The TiAl alloy and P/M superalloy served as the upper and lower samples, respectively. A normal load of 1.5 kN was applied, and friction tests were performed with a

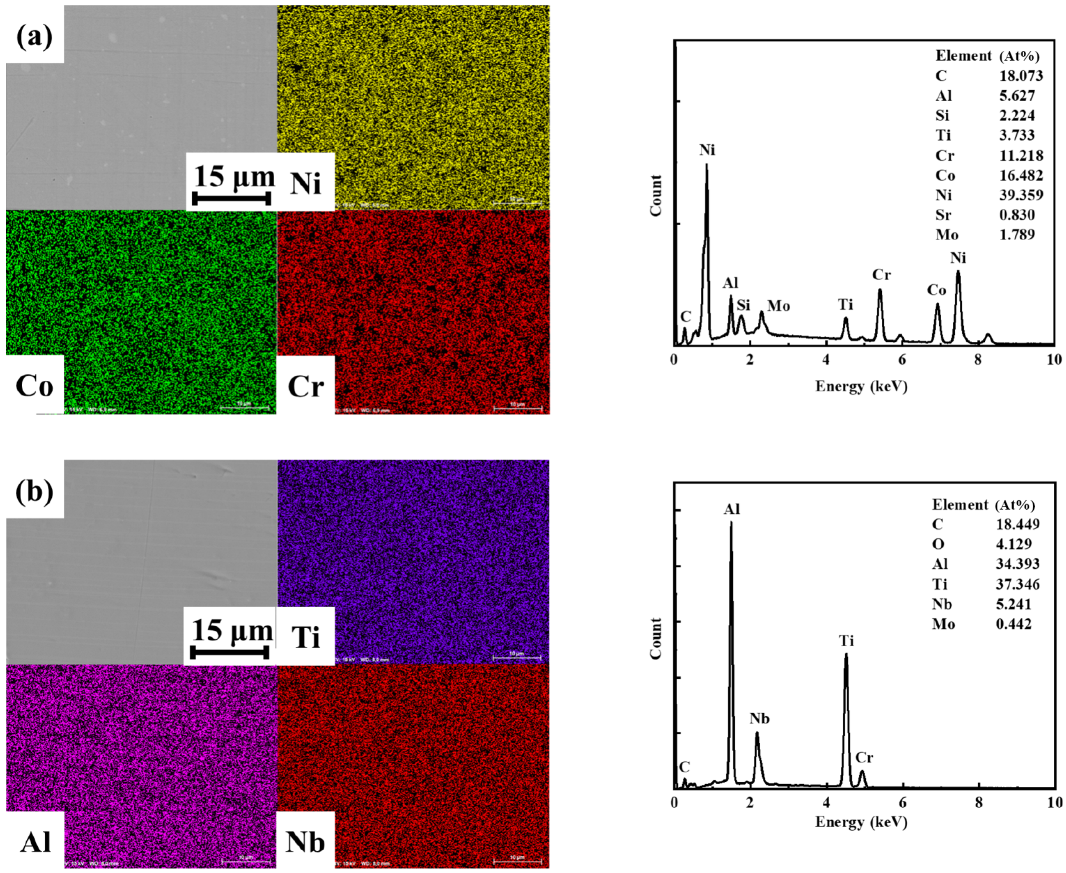

Fig. 1 EDS results for two materials: (a) P/M superalloy and (b) TiAl.

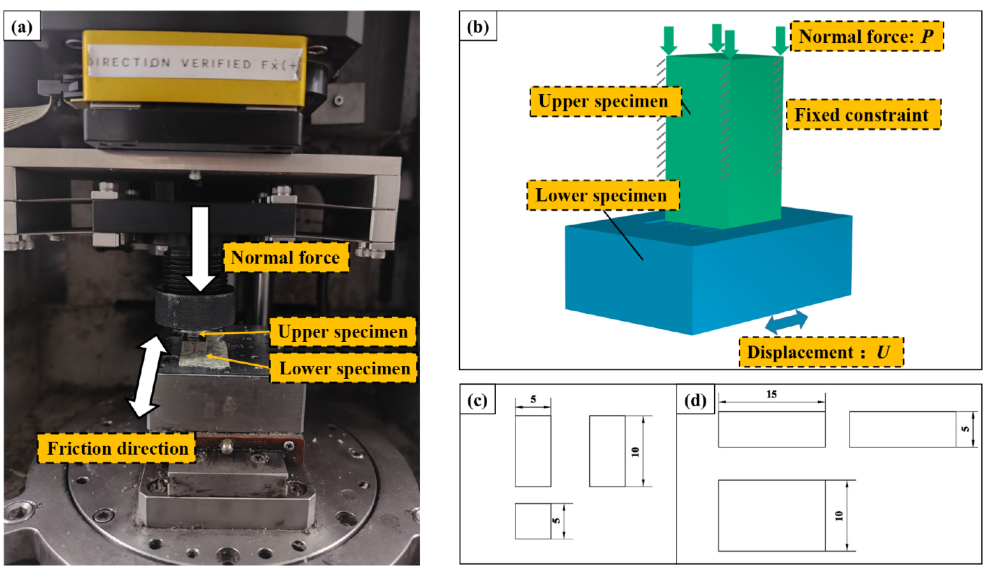

Fig. 2 Details of the test: (a) fixture diagram of the testing machine; (b) experimental device loading diagram; (c) upper sample (unit: mm); (d) lower sample (unit: mm).

2 mm stroke at 20 Hz. Tests were conducted for 24,000, 36,000, and 48,000 cycles to investigate the evolution of friction and wear mechanisms in both materials. Focusing on the lower P/M superalloy samples, friction and wear tests were conducted under varying frequencies and normal loads to explore their frictional behavior. All friction tests were performed at room temperature, and the variation in the COF with increasing number of cycles was recorded.

Prior to testing, the microhardness of both materials was measured via a microhardness tester (ZONE-DE, ZD-HVZHT-10). The P/M superalloy has a hardness of 383.4 HV0.5, which is higher than that of the TiAl alloy at 329.0 HV0.5. After testing, the samples were ultrasonically cleaned in ethanol for 5 min to remove loose wear debris from their surfaces. The material loss of the samples was subsequently quantified through morphological examinations of the postcleaning wear regions. Wear volume and depth were measured via a laser scanning confocal microscope (LSCM; Kathmatic, KC-X1000). The wear rate was calculated by dividing the wear volume by the product of the normal force and the total sliding distance. Wear scars were examined by scanning

Table 1 Test conditions

Friction stroke (mm)	Frequency (Hz)	Normal force (kN)	Upper specimen	Lower specimen	Cycle	Testing time
2					24,000	2
	20	1.5	TiAl	P/M superalloy	36,000	2
					48,000	2
					24,000	2
	20	1.5			36,000	2
					48,000	2
	20	1			36,000	1
	20	1.1			36,000	1
	20	1.2	P/M superalloy	TiAl	36,000	1
	20	2			36,000	1
	10	1.5			36,000	1
	12	1.5			36,000	1
	15	1.5			36,000	1
	18	1.5			36,000	1

electron microscopy (SEM; ZEISS, GeminiSEM300). The composition of the wear debris layer was analyzed via EDS integrated with SEM. Nanoindentation tests were performed via a nanoindenter (MML, NanoTest Vantage) with a Berkovich indenter to determine the hardness of the debris layer and compare it with that of the unworn zone.

2.2 Energy wear model considering the friction coefficient

The Archard wear model [1] is widely used to predict the amount of wear. This method relates the total amount of wear to the product of the normal force and sliding distance:

$$V = KPS \tag{1}$$

where V is the wear volume, K is the volume wear coefficient, P is the normal load, and S is the total sliding distance. However, this method does not consider the influence of friction coefficient changes during wear. To alleviate this effect, the energy wear method proposed by Fouvry et al. [2–4] and Teng et al. [5], in which the wear amount is proportional to the work done by the surface friction force, was used. Its expression is as Eq. (2):

$$V = \alpha \sum E_{\mathrm{d}} \tag{2}$$

where $\sum E_{\mathrm{d}}$ is the accumulated friction work dissipated and α is the wear coefficient of the energy method, which can be obtained by the ratio of the volume wear rate to the stable COF [25]:

$$\alpha = \frac{K}{\mu_0} \tag{3}$$

where μ_0 is the stable COF and K is the wear coefficient, which is obtained by fitting the wear volume V, normal load P, and total sliding distance S through Eq. (1).

3 Test results and discussion

3.1 Evolution of the wear scar and debris layer

Figure 3 shows some samples of the TiAl alloy and P/M superalloy before and after the test. The surface of the sample was relatively flat before the test, and black friction and wear traces appeared on the surface of the sample after the test.

Figure 3 presents representative TiAl alloy and P/M superalloy samples before and after testing. Prior to testing, the sample surfaces were relatively flat, whereas black friction and wear traces appeared on the surfaces after testing.

Figure 4 presents the optical image, SEM image, and SEM image of the edge wear debris of the wear scar in the contact area on the TiAl alloy surface after different friction test cycles with the P/M superalloy.

As shown in Fig. 4(a-1), after 24,000 friction cycles, shallow grooves appeared along the friction direction in the contact area of the TiAl alloy. Moreover, as shown in Fig. 4(a-2), aggregation of wear debris was observed at the contact edge. Enlarged images of the contact edge, shown in Fig. 4(a-3), reveal a small amount of submicron wear debris with a gradual tendency to agglomerate. The wear rate of the TiAl alloy after 24,000 cycles was 6.18× 10^{-9} $\mathrm{mm^3/(N{\cdot}mm)}$.

Figure 4(b-1) shows the contact zone morphology of the TiAl alloy after 36,000 friction cycles. The grooves in the contact area along the friction direction became deeper. At the edges of the contact area, the accumulation of wear debris increased. A micron-sized wear debris layer formed, as shown in Fig. 4(b-3). This suggests that between 24,000 and 36,000 cycles, the submicron-sized wear debris gradually accumulated at the micron scale and adhered to the contact area. Moreover, the fine debris tended to agglomerate. After 36,000 cycles, the wear rate of the TiAl alloy decreased to 4.70×10^{-9} $\mathrm{mm^3/(N{\cdot}mm)}$.

The contact area of the TiAl alloy after 48,000 friction cycles is shown in Fig. 4(c-1). At this stage, the grooves in the contact area became more pronounced. Numerous dark wear debris regions formed at the edges of the contact area, as shown in Fig. 4(c-2). Extensive wear debris accumulated to form an island-like distribution within the wear debris layer. Simultaneously, small

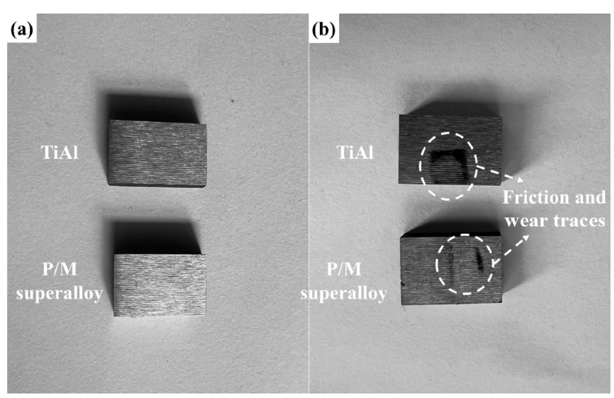

Fig. 3 Selected samples of the TiAl alloy and P/M superalloy before and after the test: (a) before the test; (b) after the test.

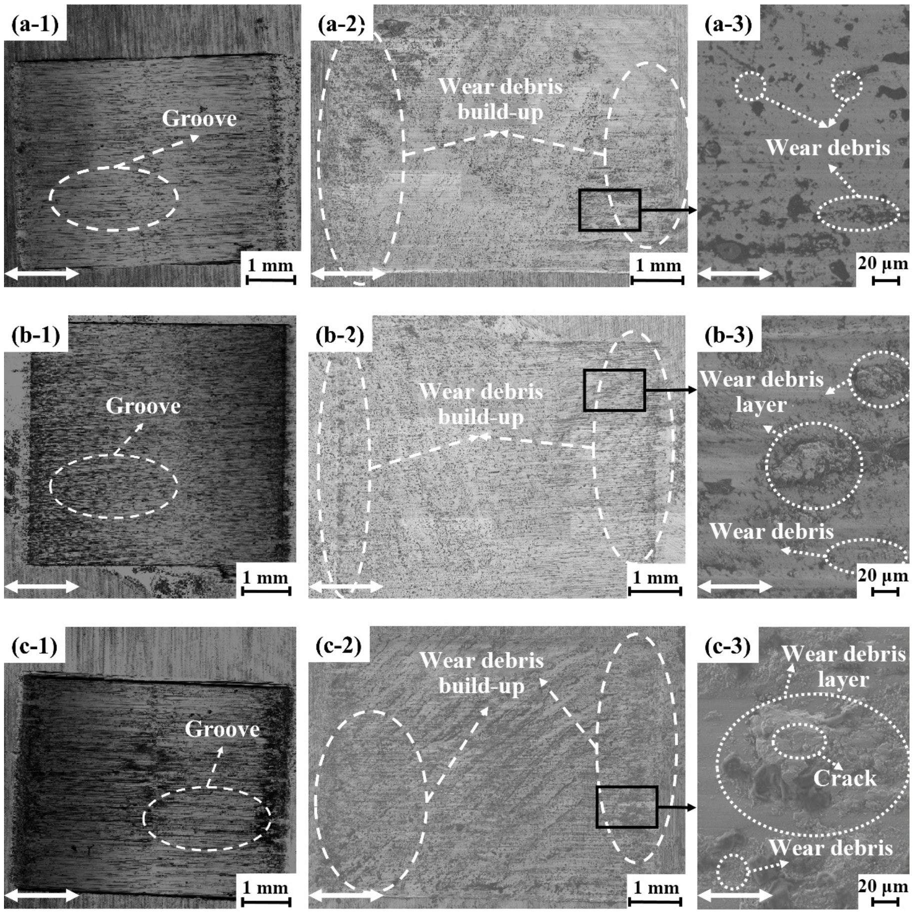

Fig. 4 (1) Optical image, (2) SEM image, and (3) SEM image of the edge wear debris of the wear scar on the surface of TiAl (upper sample: P/M superalloy): (a) 24,000 cycles; (b) 36,000 cycles; (c) 48,000 cycles.

cracks developed within the wear debris layer. This suggests that between 36,000 and 48,000 cycles, the wear debris accumulated and compacted to form a wear debris layer, which subsequently developed cracks under tangential loading, leading to wear of the TiAl alloy in the contact area. At this stage, the wear rate increased to 5.11×10^{-9} mm^3/(N·mm).

Figure 5 presents the optical image, SEM image, and SEM image of the edge wear debris of the wear scar on the contact area of the P/M superalloy surface after different friction test cycles.

After 24,000 friction cycles, owing to the high hardness of the P/M superalloy, only shallow wear marks along the friction direction were observed in the contact area, as shown in Fig. 5(a-1). Certain areas did not even obscure the original surface processing marks, as shown in Fig. 5(a-2). Upon magnified observation of the wear scar, a large amount of debris was found to accumulate, forming block-like aggregates. The wear rate was 3.04×10^{-10} mm^3/(N·mm).

Figure 5(b-1) shows the morphology of the friction region of the P/M superalloy after 36,000 friction cycles. With the accumulation of friction cycles, the edges of the friction area became increasingly distinct. As shown in Fig. 5(b-2), more wear debris was observed in the central and edge regions of the contact zone. The magnified observations of the contact area revealed that the wear debris had compacted to form a dense layer covering the P/M superalloy surface. A small amount of fine wear debris was also present on the contact surface, which ploughed the underlying material. At this stage, the wear rate increased to 5.32×10^{-10} mm^3/(N·mm).

After 48,000 friction cycles, the area of accumulated wear debris within the contact zone increased, as shown in Figs. 5(c-1) and 5(c-2). The friction contour became more distinct. Magnified observations of the debris accumulation area revealed that the wear debris was compacted within the contact zone and adhered to the surface. This suggests that between 36,000 and 48,000 friction cycles, small amounts of wear debris accumulated and compacted on the contact area surface, forming a wear debris layer that partially mitigated wear. At this stage, the wear rate slightly decreased to 4.39×10^{-10} mm^3/(N·mm).

Figure 6 shows the variations in the wear rate for the two friction pairs. As the number of friction cycles increased, the wear rate of the TiAl alloy initially decreased but then increased, whereas that of the P/M superalloy initially increased before subsequently declining. This behavior is likely attributed to the formation and subsequent fracture of the wear debris layer.

3.2 Evolution of wear debris

EDS was employed to observe and analyze the wear debris in the contact area at 5,000× magnification. The EDS results of the wear debris on the TiAl alloy surface are presented in Fig. 7. After 24,000 cycles, as shown in Fig. 7(a), numerous submicron wear debris particles were observed, gradually beginning to aggregate. The wear debris primarily consisted of oxidized Ti and Al. Additionally, small amounts of Ni, Co, and Cr were also detected in the wear debris. These observations indicate that material transfer occurred, with Ni and Cr from the P/M superalloy transferring to the wear debris and undergoing oxidation. The wear debris after 36,000 cycles is shown in Fig. 7(b). The wear debris had accumulated to form a micron-sized wear debris layer,

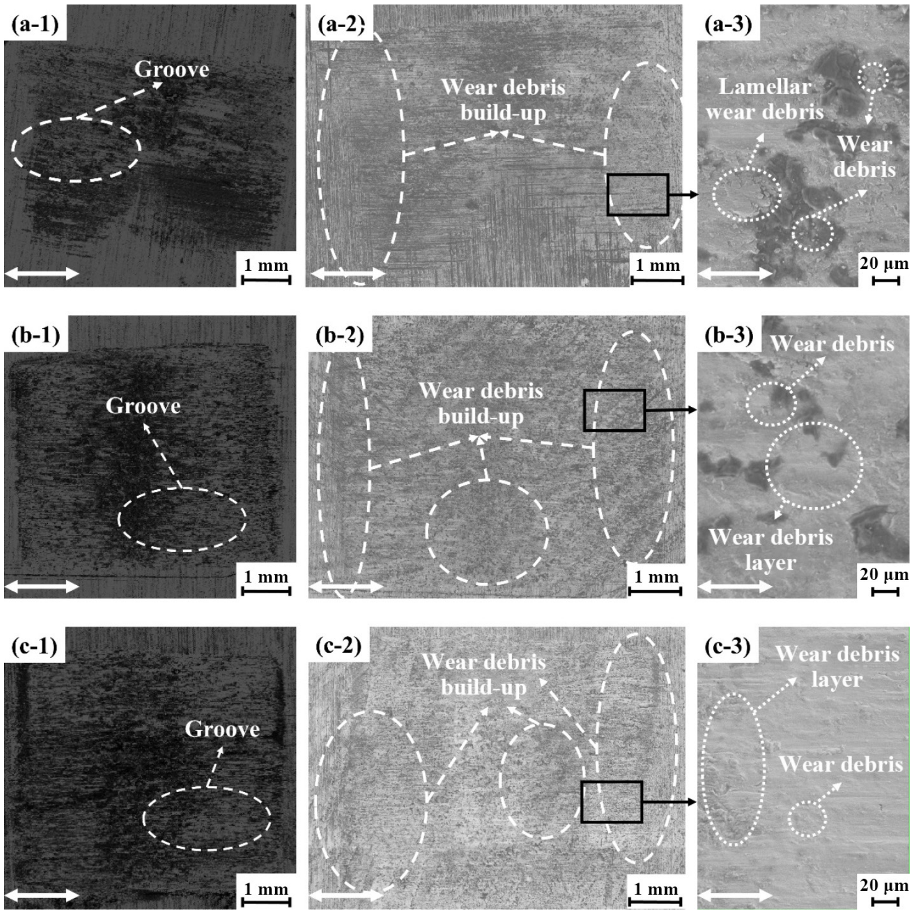

Fig. 5 (1) Optical image, (2) SEM image, and (3) SEM image of the edge wear debris of the wear scar on the surface of the P/M superalloy (upper sample: TiAl): (a) 24,000 cycles; (b) 36,000 cycles; (c) 48,000 cycles.

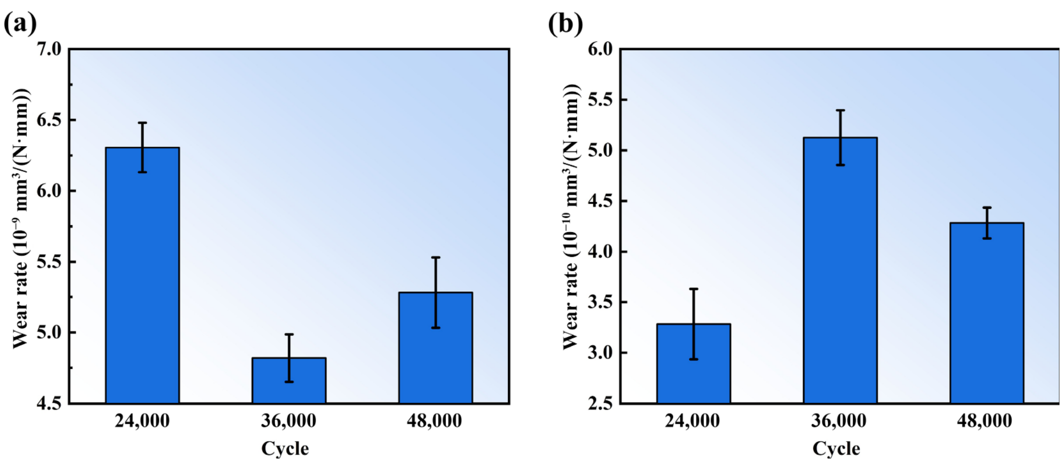

Fig. 6 Evolution of the wear rate: (a) TiAl alloy; (b) P/M superalloy.

with small cracks observed within the layer, indicating the onset of disintegration. The concentrations of Ni, Co, and Cr in the wear debris layer increased. A composite wear debris layer comprising oxides of Ti, Al, Ni, Co, and Cr formed. After 48,000 cycles, with the emergence of a small amount of fine wear debris, the wear debris layer was disrupted along the friction direction, as shown in Fig. 7(c). The concentrations of Ni, Co, and Cr in the wear debris layer decreased, indicating a reduction in the composite wear debris layer comprising oxides of all five elements. Only Ti and Al oxides remained predominantly in the wear debris.

The EDS results of the wear debris on the surface of the P/M superalloy are presented in Fig. 8. As shown in Fig. 8(a), after 24,000 friction cycles, the wear debris gradually accumulated, forming a lamellar structure. The EDS results indicate that elements from TiAl were transferred to the P/M superalloy, resulting in the formation of composite wear debris with a block-like distribution; however, a continuous wear debris layer was not observed. After 36,000 cycles, most of the wear debris had aggregated into a micron-sized wear debris layer, although some fine debris particles remained, as shown in Fig. 8(b). The concentrations of Ti and Al in the wear debris increased, indicating further material transfer from the TiAl alloy, which facilitated the formation of the composite wear debris layer. As friction continued, after 48,000 cycles, the wear debris accumulated into a dense layer, which adhered to the surface. Almost no fine debris particles were observed, as shown in Fig. 8(c).

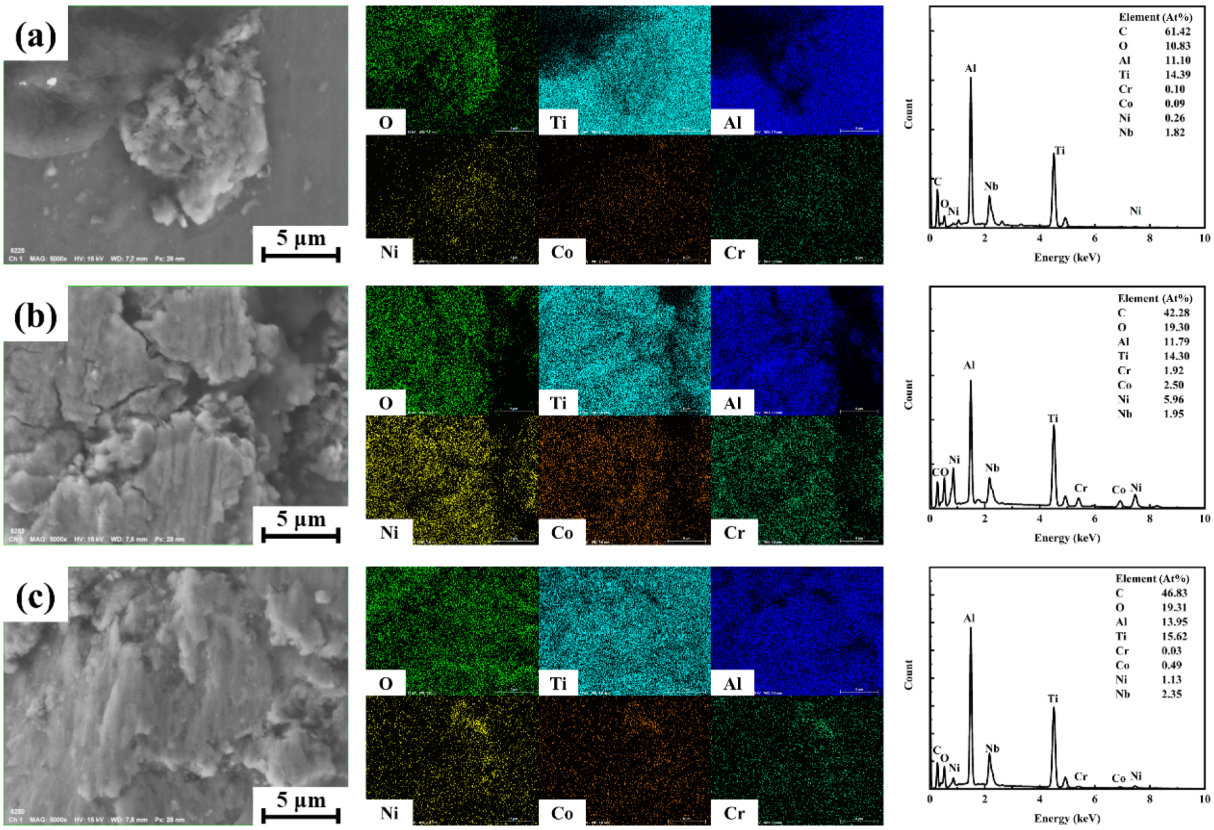

Fig. 7 Surface wear debris morphology and EDS results of TiAl: (a) 24,000 cycles; (b) 36,000 cycles; (c) 48,000 cycles.

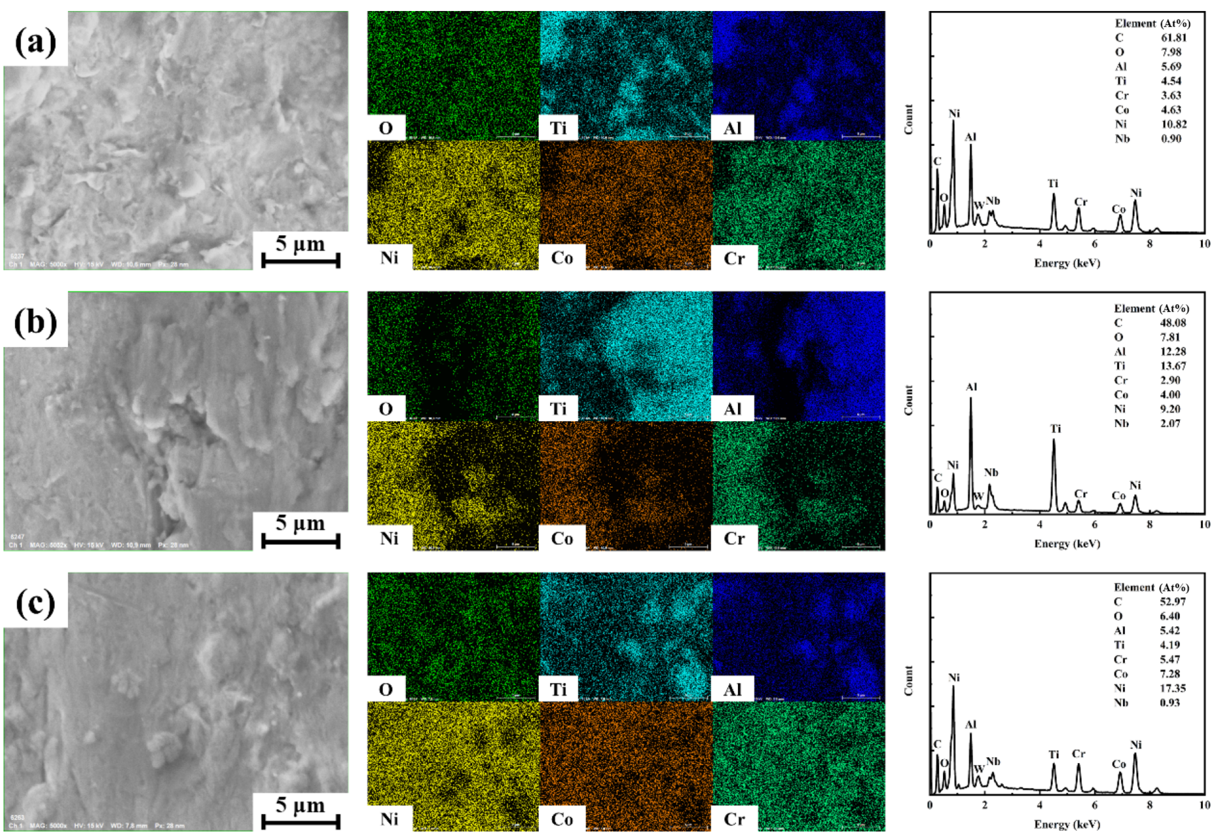

Fig. 8 Surface wear debris morphology and EDS results of the P/M superalloy: (a) 24,000 cycles; (b) 36,000 cycles; (c) 48,000 cycles.

The composite wear debris layer formed as a result of the oxidation of the P/M superalloy wear debris combined with the transferred Ti and Al.

Nanoindentation tests were performed on both the surfaces and the wear debris of the two materials [26], and the corresponding load–displacement curves are presented in Fig. 9. The measured hardness values are presented in Fig. 9(b) and summarized in Table 2. The unworn surface of the P/M superalloy has a hardness of 7.24 GPa, which is greater than that of the TiAl alloy (5.85 GPa), which is consistent with the microhardness measurements. After wear, the hardness of the wear debris on the P/M superalloy surface increased to 10.13 GPa, whereas that of the TiAl alloy increased to 9.49 GPa, both of which surpassed their original hardness values.

3.3 Friction and wear

During the friction tests between the TiAl alloy and the P/M superalloy, the variation in the COF with the number of cycles is presented in Fig. 10. The trend of the COF variation recorded during the friction tests for both materials over different cycles exhibited good consistency.

At the beginning of the test, the friction coefficient of the TiAl alloy fluctuated significantly between 0.15 and 0.35. After approximately 2×10^4 cycles, the fluctuation range of the COF decreased and gradually stabilized at a value of 0.25. During the first 2×10^4 cycles, the fluctuation range of the COF exceeded the eventual stable value. At the beginning of the test, the COF of the P/M superalloy fluctuated between 0.15 and 0.22. After 2×10^4 cycles, the fluctuation range of the COF decreased and gradually stabilized at 0.22. Once stabilized, the COF of TiAl remained higher than that of the P/M superalloy, despite reaching a steady state sooner. Prior to stabilization, however, TiAl experienced larger fluctuations that exceeded its final steady-state value.

The wear depth of the contact surfaces was measured, and the results are presented in Fig. 11. After wear, both materials exhibited a "W"-shaped profile along the friction direction. After 48,000 cycles, the TiAl wear zone exhibited a surface roughness (*Sa*) of 10.17 μm, whereas the corresponding wear region on the P/M superalloy displayed a lower *Sa* of 2.99 μm. Combined with the EDS results, these findings demonstrated that adhesive wear occurred, accompanied by material transfer on the contact surfaces. The wear depth on the TiAl surface was significantly greater than that on the P/M superalloy, resulting in a pronounced topographical difference across the surface. The wear volumes of the two materials over three cycle intervals were measured, and the product of the normal load and total sliding distance was subsequently calculated. The average wear rates of the two materials were estimated by fitting the measured data [27]. The fitting results are presented in Fig. 12. Figures 12(a) and 12(b) present the fitting outcomes for the TiAl and P/M superalloy, respectively, under different cycle counts, whereas Fig. 12(c) compares the average wear rates of the two materials. Owing to its lower hardness, the average wear rate of TiAl was 5.13×10^{-9} $mm^3/(N\cdot mm)$, which was substantially greater than that of the P/M superalloy, which was 4.45×10^{-10} $mm^3/(N\cdot mm)$.

The results of the COF for the P/M superalloy under various frequencies and normal loads are presented in Fig. 13. The diagram indicates that the COF gradually increased to a stable value under different operational conditions. Lower normal loads were associated with larger fluctuations in the COF, suggesting that reduced contact pressure was insufficient to effectively compact the wear debris. Consequently, continuous surface ploughing occurred during friction, destabilizing the surface conditions and resulting in more pronounced fluctuations in the COF. Figure 14 shows that with increasing normal load, the stable COF gradually decreased. Similarly, with increasing frequency, the stable COF also decreased, which is consistent with the findings reported in Ref. [28].

Wear depth measurements of the P/M superalloy under various loads are presented in Fig. 15. The wear depth gradually increased with increasing load. Under a normal load of 1 kN, the wear depth was 8.49 μm. When the load increased, the wear depth gradually reached 10.95 μm under identical friction cycles. At a load of 1.5 kN, as previously mentioned, the wear depth reached

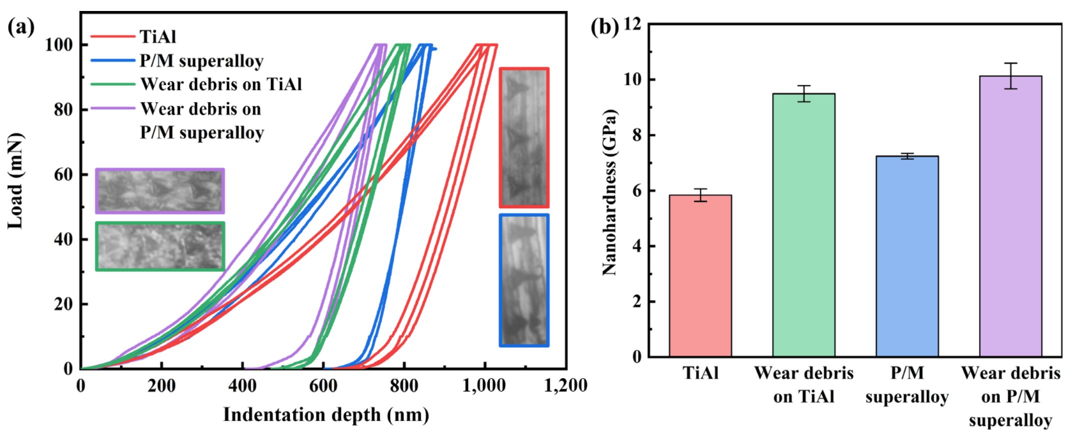

Fig. 9 Nanoindentation test results: (a) nanoindentation load–depth curves of the wear debris and original material; (b) hardness values.

Table 2 Nanoindentation hardness (Unit: GPa)

	Test 1	Test 2	Test 3	Average
TiAl	5.63	5.82	6.08	5.85
P/M superalloy	7.13	7.32	7.29	7.24
Wear debris on TiAl	9.26	9.82	9.40	9.49
Wear debris on P/M superalloy	10.62	9.70	10.07	10.13

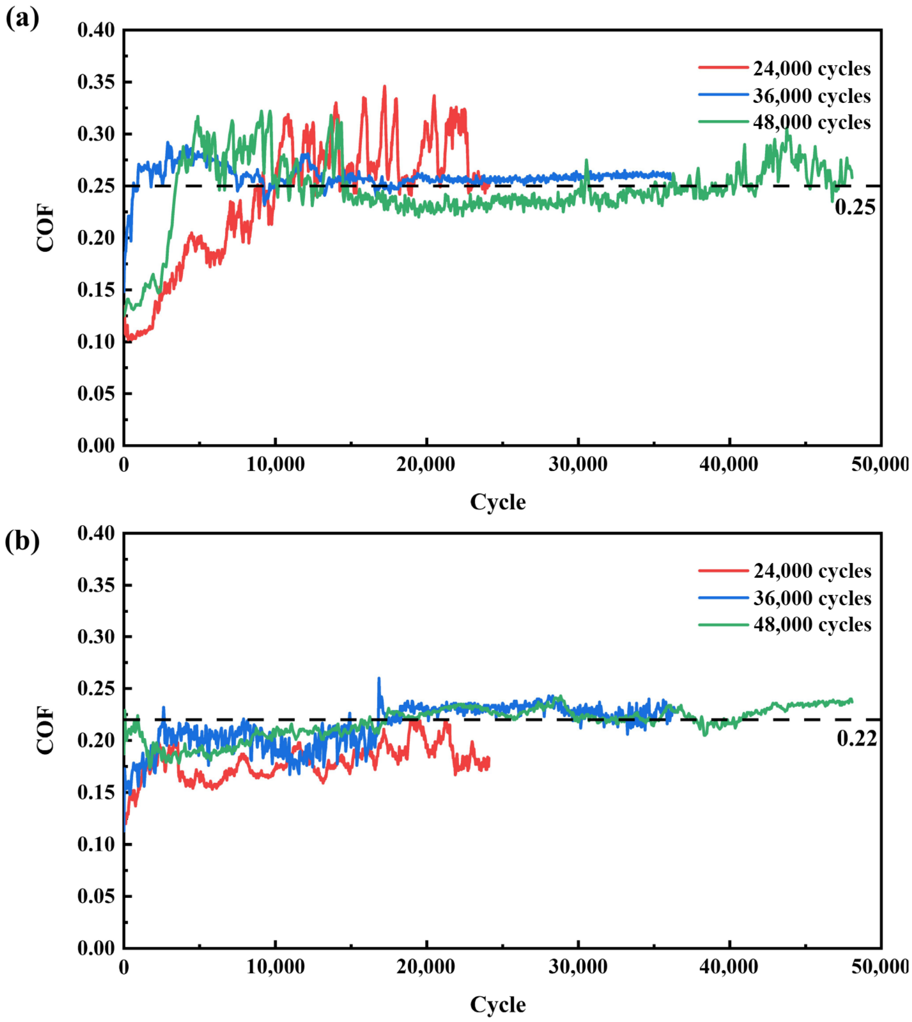

Fig. 10 The variation in the COF with the number of cycles: (a) TiAl; (b) P/M superalloy.

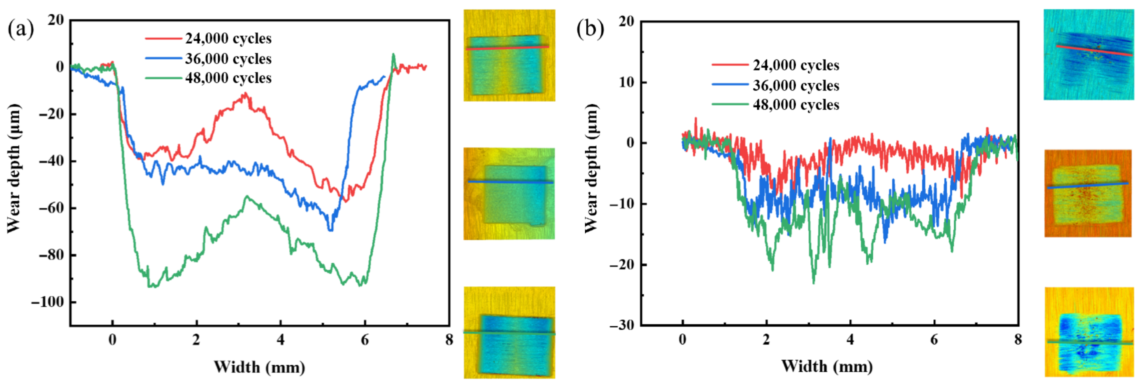

Fig. 11 Wear depth: (a) TiAl; (b) P/M superalloy.

13.85 μm. Concurrently, with increasing load, the wear area gradually stabilized, the central bulge diminished, and the edge contour of the wear region became more distinct.

3.4 Discussion

The observed wear characteristics of the two materials were used. Owing to the lower initial hardness of the TiAl surface than that of the P/M superalloy, the wear marks were pronounced and easily distinguishable, with relatively large wear depths and wear rates. Throughout the entire test, wear debris was observed both within the contact surface and between the two contacting surfaces, forming a typical three-body wear mechanism. The wear debris layer on the TiAl surface underwent a progression from aggregation to compaction, followed by disintegration. In contrast, the wear debris on the surface of the P/M superalloy did not disintegrate throughout the test.

In the initial stage, portions of the TiAl surface generated fine, high-hardness wear debris. Some of this debris induced ploughing on the contact surfaces, leading to an elevated wear rate during the early stage. At this stage, the wear debris primarily functions as sliding abrasives on the contact surfaces, with cutting wear as the dominant mechanism. As friction progressed, the wear debris

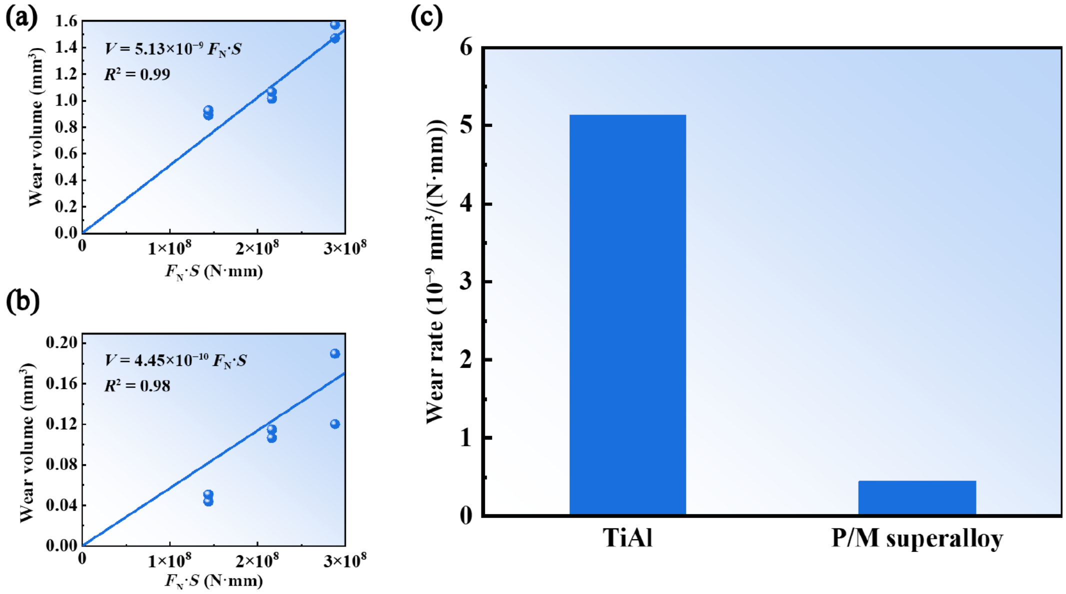

Fig. 12 Average wear rate: (a) fitting results of TiAl; (b) fitting results of the P/M superalloy; (c) comparison of the average wear rate.

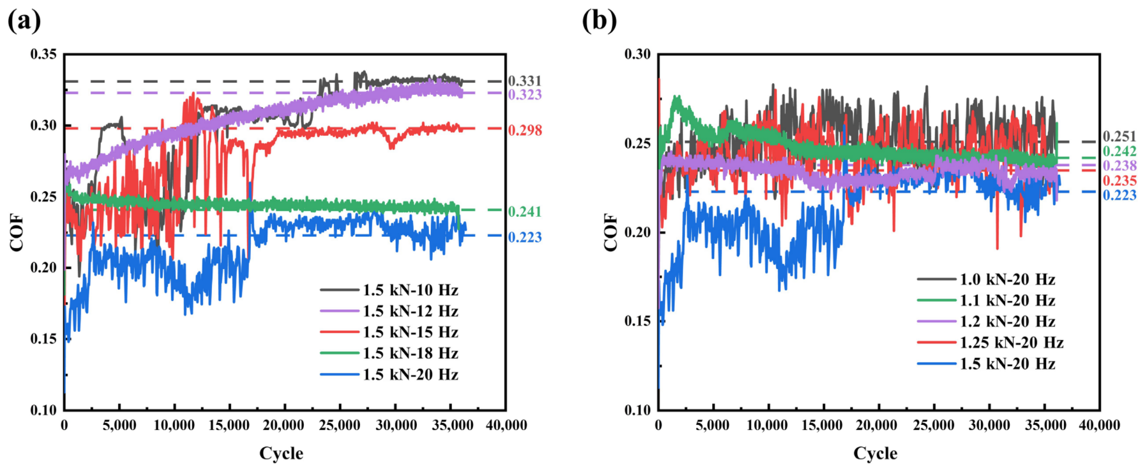

Fig. 13 COF of P/M superalloy under different working conditions as a function of the number of cycles: (a) different frequencies; (b) different normal pressures.

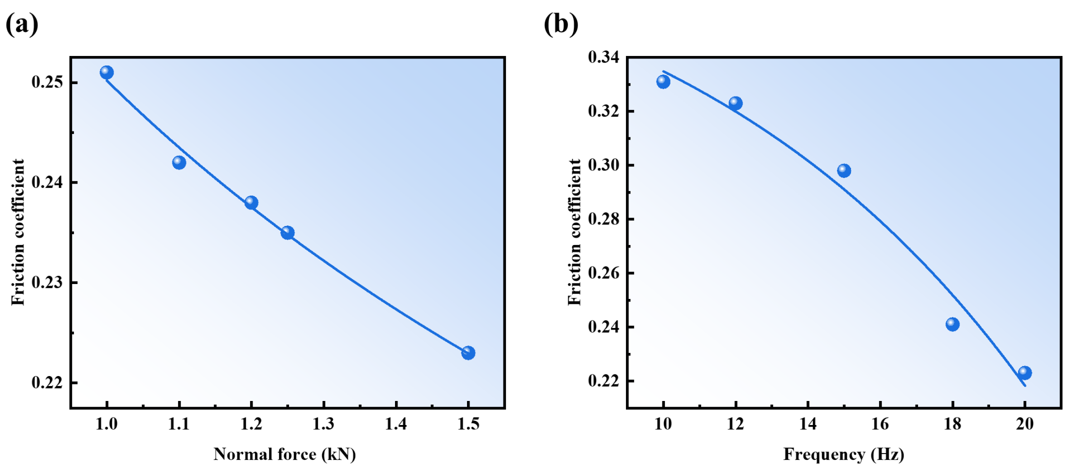

Fig. 14 COF of P/M superalloy under different stable working conditions: (a) different normal loads; (b) different frequencies.

transitioned from sliding to rolling abrasives on the contact surfaces, thereby weakening the ploughing effect. A fraction of the debris accumulated to form a micron-scale, high-hardness composite layer, consequently reducing the wear rate. Concurrently, the dominant wear mechanism shifted from cutting wear to oxidative wear. The debris layer subsequently aggregated into island-like structures before disintegration. Debris that failed to integrate into the composite layer acted as rolling abrasives. Through repeated lapping, these abrasives further fragmented the debris layer. The high-hardness debris adhered to the contact

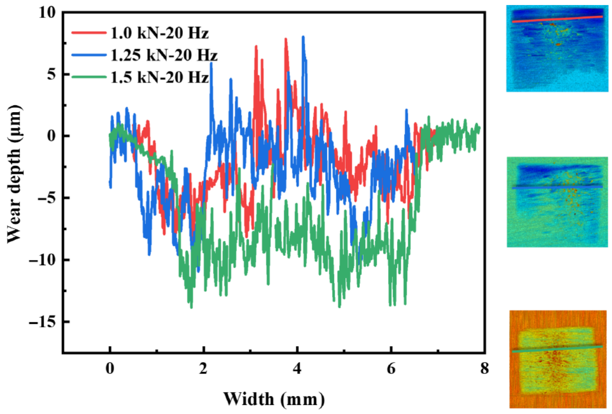

Fig. 15 Wear depth of P/M superalloy under different loads.

surfaces, functioning as sliding abrasives that induced additional wear and increased the wear rate. The wear mechanism reverted to a combination of plastic deformation and cutting wear. Simultaneously, following the rapid formation of the surface wear debris layer, it fractured again, resulting in instability of the friction state in the contact area and causing significant fluctuations in the friction coefficient. Compared with the P/M superalloy, TiAl exhibited a lower hardness, more severe surface wear, and greater surface roughness, resulting in a higher steady-state friction coefficient.

Initially, material transfer occurred on the surface of the P/M superalloy, causing TiAl debris from the grinding material to adhere to the contact surface, where it subsequently underwent oxidation. The high-hardness composite debris functioned as sliding abrasives, inducing additional surface ploughing and thereby increasing the wear rate. During this phase, the dominant wear mechanisms were oxidative wear and abrasive cutting wear. A portion of the composite wear debris subsequently transitioned into rolling abrasives. These particles accumulated and compacted on the contact surface, ultimately forming a protective composite debris layer, which reduced the wear rate. During this stage, plastic deformation wear emerged as the primary mechanism. The gradual development of this debris layer throughout the testing process facilitated a stable friction state, resulting in minimal fluctuations in the friction coefficient. In summary, the evolution of the contact surfaces of the two materials during the grinding process is illustrated in Fig. 16. High-hardness oxidized composite wear debris formed on the contact surfaces. On the one hand, ploughing occurred on the contact surfaces, resulting in an increased wear rate. On the other hand, as friction continued, the debris gathered and compacted on the contact surfaces, forming a high-hardness composite wear debris layer that adhered to the surface and partially reduced the wear rate. As friction continued, the debris layer on the surface fractured, and the broken high-hardness debris continued to induce additional ploughing between the contact surfaces, thereby increasing the wear rate. The two samples, together with the wear debris, formed a three-body wear system, in which the abrasive particles underwent sliding–rolling motion during friction. This motion resulted in a progressive change in the wear rate as the process continued.

4 Energy wear model considering friction coefficient differences

4.1 Simulation details

In the energy-based wear method, the friction coefficient influences the computed energy wear coefficient, potentially causing deviations in the calculated wear volume. Therefore, the choice of friction coefficient under varying normal loads significantly affects the wear calculation results. The variation in the friction coefficient under different operating conditions observed in this study indicates that the stable friction coefficient gradually decreases with increasing normal load. Moreover, with increasing sliding frequency, the stable friction coefficient also decreases, which is consistent with the findings reported in Ref. [28]. As the normal load increases, asperity deformation on the material surface intensifies, resulting in reduced surface roughness and a corresponding decrease in the friction coefficient. With increasing friction frequency, the contact duration of surface asperities decreases, which inhibits material adhesion and allows more complete stress relaxation of the asperities. Furthermore, high-frequency friction generates more heat, increasing the surface temperature, which softens the material and reduces its hardness. Consequently, the friction coefficient decreases.

The stable COF varies in response to changes in external operating conditions. The observations indicate that the COF decreases with increasing normal load and sliding frequency [28]. Wang et al. [25] proposed a wear model incorporating the effect of wear debris and applied it to calculate the wear curve of

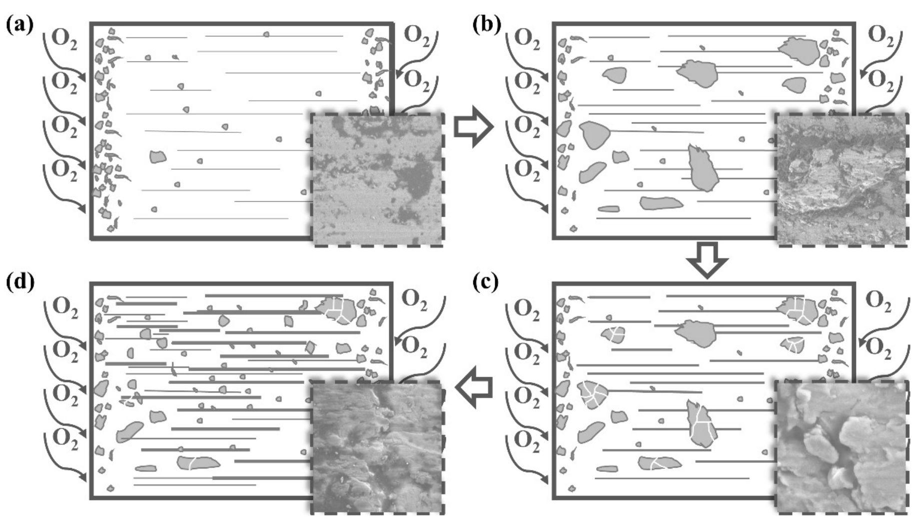

Fig. 16 Evolution of wear debris in the contact zone: (a) high-hardness oxidation composite wear debris; (b) grinding debris layer formation; (c) debris layer rupture; (d) a large amount of debris produces ploughing.

清華大学出版社 Tsinghua University Press | SciOpen

aluminum 2024-T351. Baydoun et al. [29] developed an energy-based wear model accounting for the influence of contact size and slip amplitude and subsequently calculated the wear rate of 34NiCrMo16. Arnaud et al. [30] proposed a fretting wear model incorporating third-body evolution and computed the wear rate of the Ti–6Al–4V cylinder/plane interface with an error of less than 10%. Yang et al. [31] established a fretting wear model incorporating the effects of friction layer formation and validated it via wear models for different contact types. Springis and Boiko [32] proposed an integrated approach that combines probabilistic surface modeling, fatigue-based degradation theory, and numerical simulation to improve wear prediction, addressing the limitation that classical wear models insufficiently account for material fatigue and 3D surface texture parameters. Wang et al. [33] proposed an improved theoretical model of nodal energy-dissipation wear and designed an acoustic emission-based wear-fatigue detection platform for dynamic shaft rotation to verify the model. However, in the aforementioned studies, the friction coefficient was assumed to be a fixed value under varying operating conditions, which may result in simulation outcomes that fail to accurately reflect actual working conditions. On the basis of the findings reported in Ref. [34], the COF has an exponential correlation with the linear velocity.

$$\mu_0 \propto \exp(-cv) \tag{4}$$

where v is the linear velocity of friction and c is a constant. The linear velocity can be expressed as $v = 2A \cdot f$ by the frequency and friction stroke, where A is the friction stroke and f is the friction frequency.

The relationship between the friction coefficient and normal load is hyperbolic [28].

$$\mu_0 \propto P^{-b} \tag{5}$$

In Eq. (5), P is the normal load and b is the undetermined exponential constant. Therefore, the model of the whole stable friction coefficient can be expressed as

$$\mu_0 = a \cdot P^{-b} \cdot \exp(-cv) = a \cdot P^{-b} \cdot \exp(-2cAf) \tag{6}$$

The constants a, b, and c are obtained via experimental fitting. Furthermore, the wear coefficient α of the energy method can be expressed as

$$\alpha = \frac{K}{a \cdot P^{-b} \cdot \exp(-2cAf)} \tag{7}$$

The wear model considering the change in the friction coefficient under different loads is obtained by introducing Eq. (7) into Eq. (2):

$$V = \frac{K}{a \cdot P^{-b} \cdot \exp(-2cAf)} \sum E_{\mathrm{d}} \tag{8}$$

Building upon the original model, the wear model is extended to predict wear under varying normal loads and sliding frequencies.

Three sets of test results of the P/M superalloy under different working conditions were used for fitting, and the results of the three parameters $a = \mathrm{e}^{0.98702}$, $b = 0.22681$, and $c = 0.01004$ in Eq. (6) were obtained by verifying the stable COFs of the other two groups.

$$\mu = \mathrm{e}^{0.98702} \cdot P^{-0.22681} \exp(-0.02008Af) \tag{9}$$

The local energy-based wear method can be applied to the entire contact interface to calculate the local wear depth at each contact point. The corresponding local wear model is formulated as Eq. (10):

$$\Delta h(x) = \alpha \int_{i=0}^{n} q(x,i)\, \mathrm{d}s(x,i) \tag{10}$$

where $\Delta h(x)$ is the total wear depth in n time periods; $q(x,i)$ and $s(x,i)$ are the shear stress and slip distance, respectively, of the contact surface nodes numbered as x at time i; and α is the energy wear coefficient. In this way, the wear depth of each node in the contact zone in any time period can be calculated in the finite element.

Equation (10) is discretized. Assuming that each analysis step has n simulation increments, the total wear depth in an analysis step can be approximated as

$$\Delta h(x) = \alpha \sum_{i=1}^{n} q(x,i)\, \Delta s(x,i) \tag{11}$$

where $\Delta h(x)$ is the wear depth of the contact surface node numbered x in a friction cycle and $\Delta s(x,i)$ is the relative slip distance of the contact surface node numbered x at time i.

To simulate the wear depth efficiently, the cyclic jump technique is used [35]. The wear depth is considered to increase linearly within a certain cycle ΔN. The wear depth $\Delta h(x)$ of the corresponding ΔN fretting cycles can be simulated in an analysis step using Eq. (12):

$$\Delta h(x) = \Delta N \cdot \alpha \sum_{i=1}^{n} q(x,i)\, \Delta s(x,i) \tag{12}$$

The size of the periodic cycle increment, ΔN, significantly influences both the stability and accuracy of the analysis. As expected, smaller values of ΔN yield more accurate results but at the expense of increased computational time and memory requirements. In this study, the cyclic increment ΔN is set to 1,000, which balances computational efficiency with analytical stability and accuracy. At the end of each convergent increment in the finite element calculation, the wear depth at each node on the contact surface is determined via the shear stress, slip amplitude, and energy-based wear coefficient corresponding to that node during the increment. Within an adaptive meshing framework, the displacement of constraint nodes perpendicular to the contact surface is subsequently restricted, thereby modifying the shape of the contact area and, in turn, altering the stress state of the contact interface.

The COFs for the five groups of P/M superalloy under different operating conditions were calculated, and the results are presented in Table 3. The analysis indicates that the discrepancy between the COFs predicted via the fitting equation (9) and the experimentally measured COF remains within 10%. Consequently, the proposed model can be reliably employed to estimate the COF of P/M superalloy under varying working conditions, thereby enabling correction of the wear model across different operational scenarios.

In finite element analyses, an accurate definition of the contact behavior is essential. The change in the COF over friction time must be considered [36]. The experimental observations indicate that the COF increases approximately exponentially with increasing number of cycles. Accordingly, an exponential function is employed to characterize the COF as a function of the cycle count. For the TiAl alloy, this relationship can be expressed as Eq. (13):

$$\mu(N) = -0.13303\mathrm{e}^{-\frac{N}{5804}} + \mu_0 \tag{13}$$

For the P/M superalloy, the relationship can be expressed as Eq. (14):

$$\mu(N) = -0.06245\mathrm{e}^{-\frac{N}{18412}} + \mu_0 \tag{14}$$

In Eqs. (13) and (14), μ_0 is the COF at stabilization.

Finite element simulations were conducted via the commercial software ABAQUS to validate the proposed energy-based wear model incorporating variations in the COF. A finite element model was constructed on the basis of the experimental setup and loading conditions, as illustrated in Fig. 17(a). The bottom of the lower sample was fully constrained, whereas a normal load P was applied to the top of the upper sample. A reciprocating displacement constraint U was imposed at the right end of the upper sample, as depicted in Fig. 17(b). To increase the computational accuracy, the mesh in the vicinity of the contact surface was refined, with an element size of 0.2 mm × 0.2 mm × 0.2 mm in the contact region. The loading histories of the displacement constraint U and normal load P are presented in Fig. 17(c). During the first analysis step, the normal load P was applied to the sample and subsequently held constant. From the second analysis step onward, the displacement constraint U was imposed on the right side of the sample.

The mesh was generated via three-dimensional eight-node linear elements (C3D8). The contact interaction was defined via ABAQUS's master–slave algorithm, with the upper sample surface designated the master surface and the lower sample surface the slave surface. Finite sliding was employed to describe the relative motion between contact surfaces. The COF under various operational conditions was calculated according to Eq. (9). The wear model simulation was implemented through the UMESHMOTION user subroutine.

Table 3 Calculation results of the COF under different working conditions

Normal force (N)	Frequency (Hz)	Friction stroke (mm)	Tested COF	Calculated COF	Error (%)
1,000	20		0.251	0.2499	0.43
1,100	20		0.242	0.2455	1.48
1,200	20		0.238	0.2417	1.55
1,250	20		0.235	0.2399	2.08
1,500	10	2	0.331	0.3419	3.29
1,500	12		0.323	0.3075	4.79
1,500	15		0.298	0.2766	7.15
1,500	18		0.241	0.2489	3.30
1,500	20		0.223	0.232	4.05

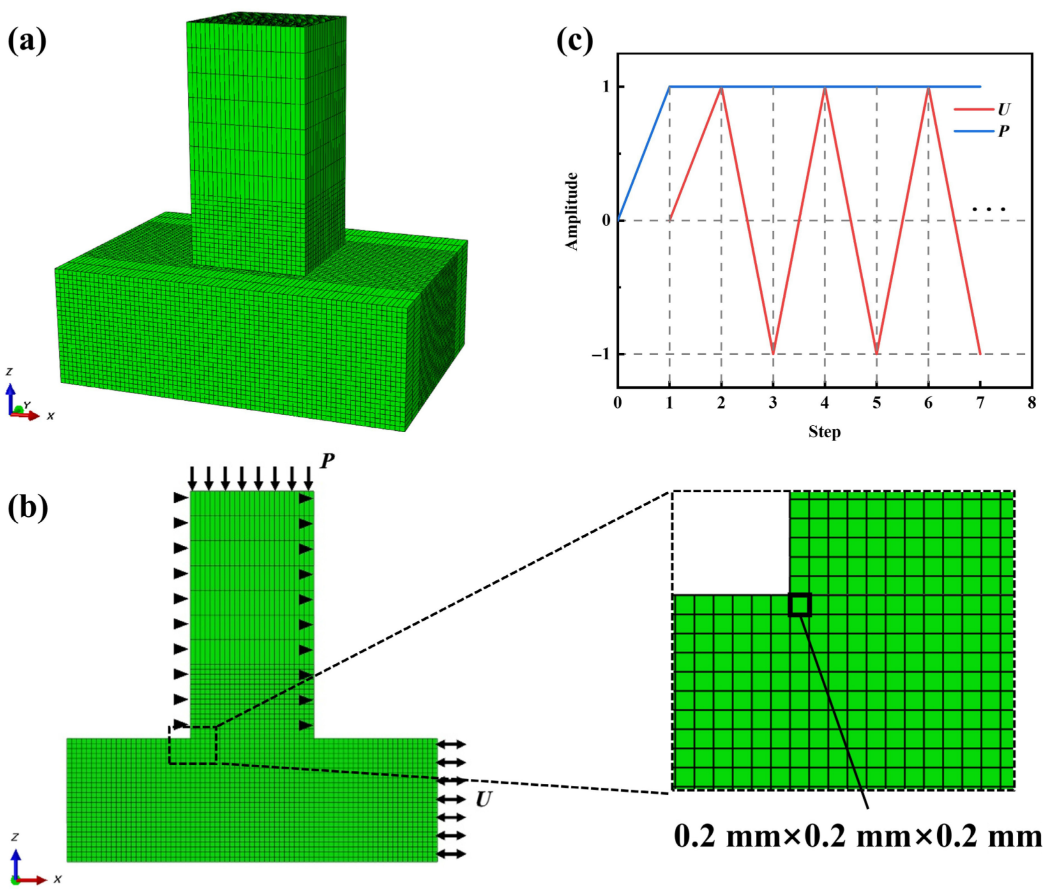

Fig. 17 Finite element model loading conditions.

清华大学出版社 Tsinghua University Press | SciOpen

The overall process of the wear simulation considering variations in the COF under different working conditions is illustrated in Fig. 18. In this study, the variation law of the friction coefficient obtained from friction and wear experiments was implemented to determine the COF as a function of the number of cycles in the simulation. The experimentally measured wear rate was used to calibrate the friction and wear model for each working condition, which then guided the calculation of the wear depth in the simulation. Initially, the COF corresponding to the actual load conditions was determined. The tangential friction behavior between contact surfaces was modeled via a penalty function formulation. During each analysis step, the COF was updated via Python scripts. The stress and strain distributions in the contact area were obtained through finite element analysis, and an energy-based wear model was employed to incrementally compute the wear depth. The geometry was updated at each step via the UMESHMOTION user subroutine until the specified number of cycles was reached, yielding the wear depth for the given operational conditions.

4.2 Wear simulation results

Since TiAl was subjected to only a single set of friction and wear tests under varying cycle numbers at constant load conditions, the friction coefficient was set to a constant value of 0.25. The von Mises stress distributions on the TiAl surface after 24,000, 36,000, and 48,000 cycles are shown in Fig. 19. The results indicate that the surface morphology evolves with the number of cycles due to wear, which in turn affects the stress distribution. Under all the examined cycles, the maximum von Mises stress on the surface does not exceed the material's yield stress, confirming that the simulation assumptions based on purely elastic material behavior are reasonable.

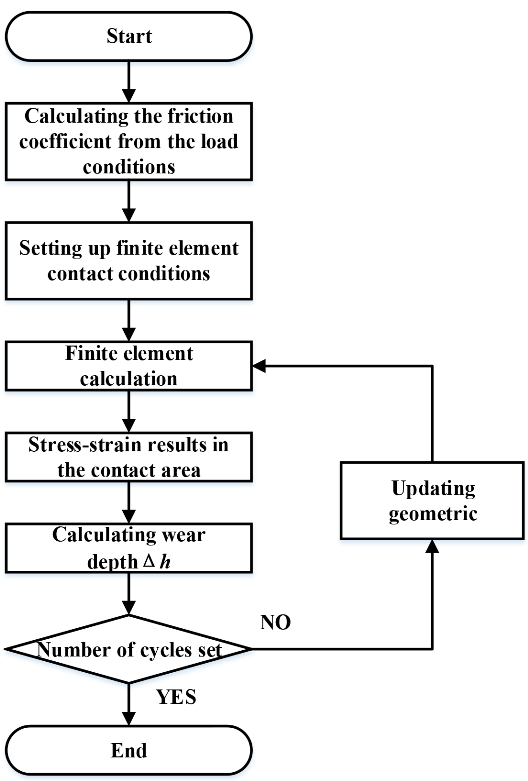

Fig. 18 Calculation flow chart of the wear simulation.

The wear depth under different numbers of cycles was calculated, as shown in Fig. 20. Figures 20(a)–20(c) present the wear depth distributions of TiAl after 24,000, 36,000, and 48,000 cycles, respectively. Figures 20(d)–20(f) compare the simulation results of the wear depth at the two edges and the center of the contact area with the experimental measurements for the corresponding number of cycles.

As shown in Fig. 20, the finite element simulation results of wear in the contact area exhibit a "W"-shaped distribution along the friction direction, which is consistent with the experimental observations. After 24,000 cycles, the wear depth measured experimentally at the center of the contact area is 57.15 μm, whereas the maximum depth predicted by the simulation is 52.21 μm, resulting in an error of 4.94 μm. After 36,000 cycles, the experimental wear depth is 69.40 μm, whereas the simulated value is 70.31 μm, with an error of 0.91 μm. At 48,000 cycles, the measured wear depth reaches 93.50 μm, and the simulated depth is 90.77 μm, yielding an error of 2.73 μm. These results demonstrate that the proposed simulation method achieves high accuracy.

Under a load of 1.5 kN and a frequency of 20 Hz, wear simulations were performed for the P/M superalloy at different cycles. According to Table 3, COF was set to 0.2288, which was calculated via Eq. (9), and the wear model was accordingly updated. The von Mises stress distributions on the surface of the P/M superalloy after 24,000, 36,000, and 48,000 cycles are shown in Fig. 21. In all the cases, the maximum equivalent stress on the sample surface remains below the material yield limit, confirming the validity of modeling the material as purely elastic in these simulations.

The wear depth under different numbers of cycles is presented in Fig. 22. Figures 22(a)–22(c) show the wear depth results of the P/M superalloy after 24,000, 36,000, and 48,000 cycles, respectively. Figures 22(d)–22(f) compare the simulation results with the experimental measurements for the two edges and the middle of the contact area under the corresponding number of cycles.

Similarly, the wear distribution in the contact area along the friction direction exhibited a "W"-shaped profile, which was consistent with the experimental observations. At 24,000 cycles, the wear depth measured in the contact area was 9.01 μm, whereas the maximum depth predicted by the simulation was 7.46 μm, resulting in an error of 1.55 μm. At 36,000 cycles, the experimental wear depth was 13.85 μm, whereas it was 11.86 μm in the simulation, with an error of 1.99 μm. At 48,000 cycles, the measured wear depth was 23.06 μm, and the simulated maximum depth was 19.33 μm, yielding an error of 3.73 μm. These results demonstrate that the wear model, which accounts for variations in the friction coefficient, can achieve high accuracy in predicting wear.

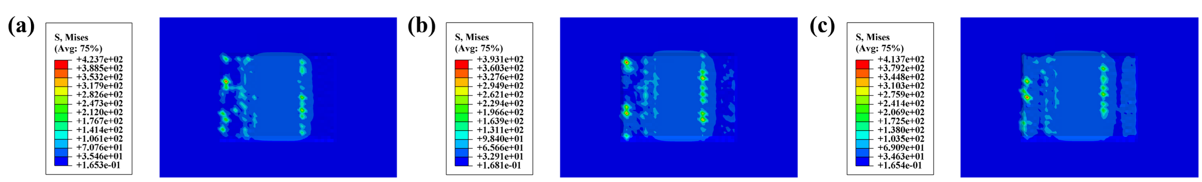

Fig. 19 Von Mises stress distributions of TiAl after different numbers of cycles: (a) 24,000 cycles; (b) 36,000 cycles; (c) 48,000 cycles.

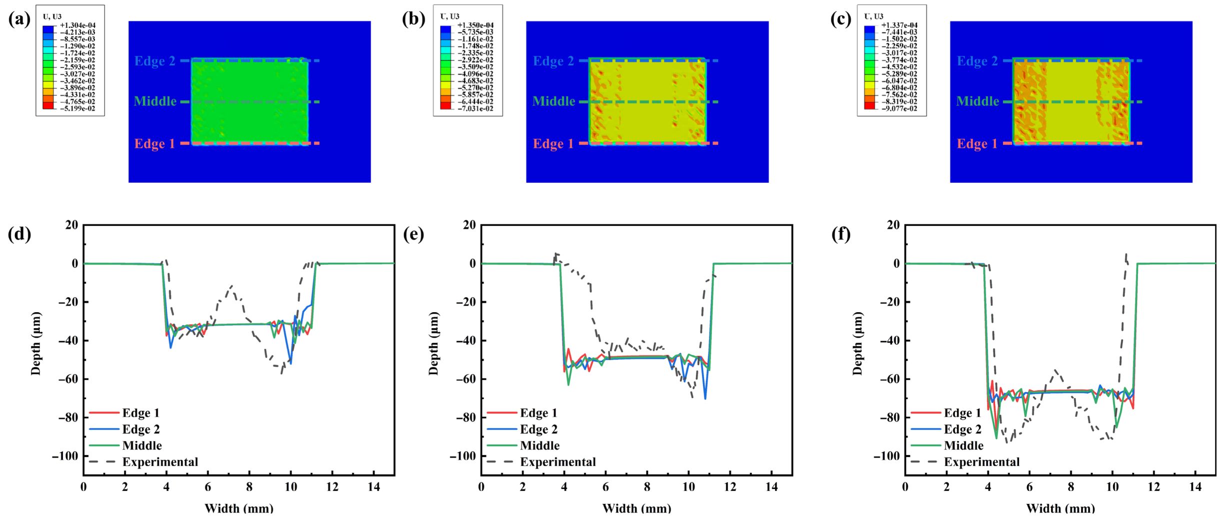

Fig. 20 Wear depth of TiAl after different numbers of cycles: (a) 24,000 cycles; (b) 36,000 cycles; (c) 48,000 cycles; and (d) 24,000 cycles compared with the test results; (e) 36,000 cycles compared with the test results; (f) 48,000 cycles compared with the test results.

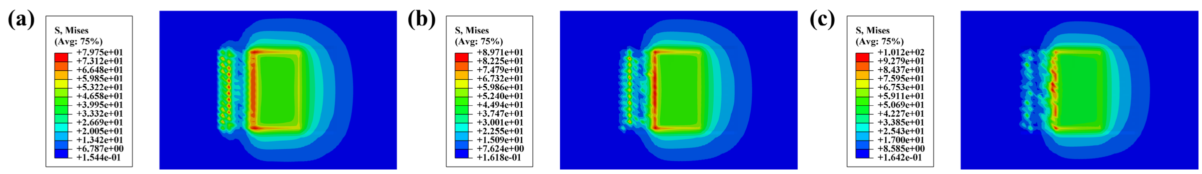

Fig. 21 Von Mises stress distributions of P/M superalloys after different numbers of cycles: (a) 24,000 cycles; (b) 36,000 cycles; (c) 48,000 cycles.

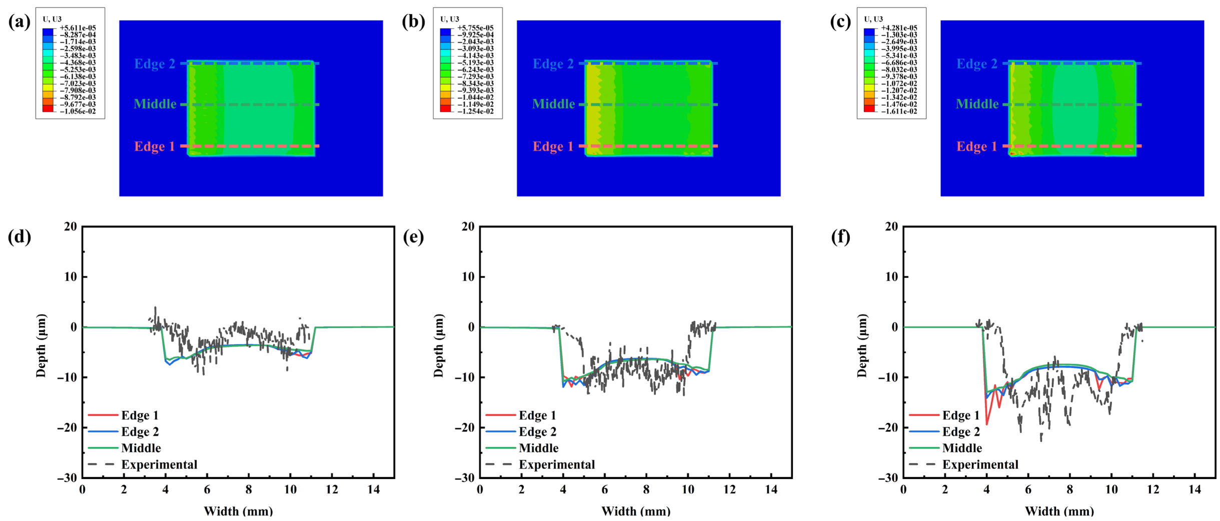

Fig. 22 Wear depths of P/M superalloys after different numbers of cycles: (a) 24,000 cycles; (b) 36,000 cycles; (c) 48,000 cycles; and (d) 24,000 cycles compared with the test results; (e) 36,000 cycles compared with the test results; (f) 48,000 cycles compared with the test results.

Under different loads, the simulation and experimental results for the P/M superalloy after 36,000 cycles are shown in Fig. 23. The wear depth in the contact zone is the smallest in the middle and largest at the edges, which is consistent with the experimental observations. When the load is 1 kN, the simulation predicts a wear depth of 8.02 μm, whereas the maximum experimental depth is 8.49 μm, resulting in an error of 0.47 μm. At 1.25 kN, the simulation yields a value of 9.97 μm, whereas the experimental measurement is 10.95 μm, with an error of 0.98 μm. These results indicate that the wear model, which accounts for variations in the friction coefficient, maintains relatively high accuracy under different load conditions. However, the simulation does not capture the observed decrease in the middle height of the contact area with increasing load.

5 Conclusions

In this work, friction and wear tests were performed on TiAl alloys and P/M superalloys to investigate their wear mechanisms. On the basis of the observed decrease in the stable COF with increasing normal load and friction frequency, an energy-based wear model incorporating COF variations under different working conditions was developed. The model was validated through a comparison with experimental results, which demonstrated good agreement. The main conclusions are summarized as follows:

(1) When the TiAl and P/M superalloy are in contact, the average wear rate of TiAl is significantly greater than that of the P/M superalloy. During the test, the wear rate of TiAl initially

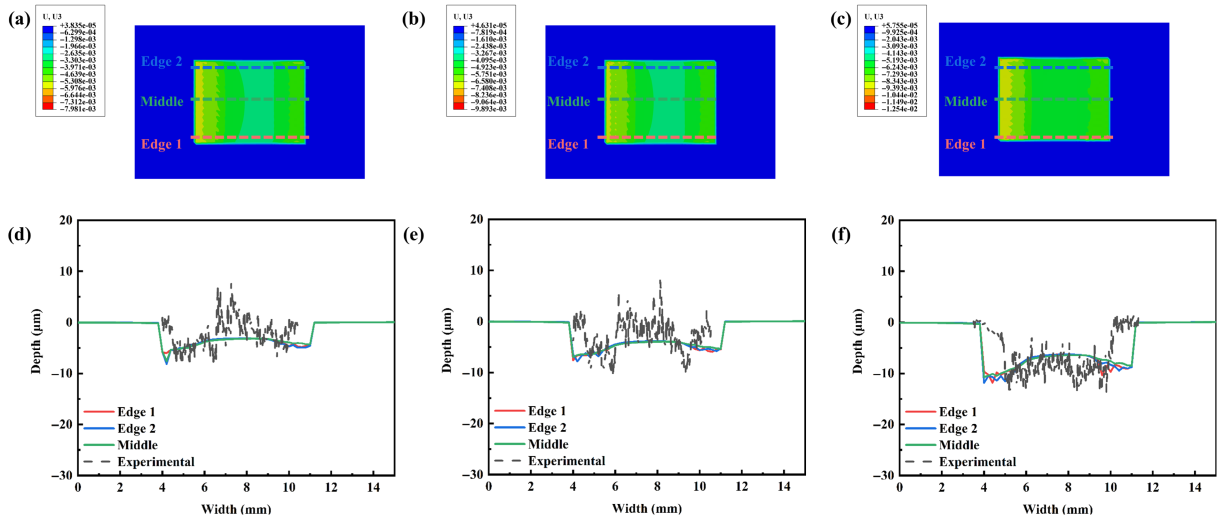

Fig. 23 Wear depth of the P/M superalloy under different loads: (a) 1 kN; (b) 1.25 kN; (c) 1.5 kN; and (d) 1 kN compared with the test results; (e) 1.25 kN compared with the test results; (f) 1.5 kN compared with the test results.

decreased from 6.18×10^{-9} to 4.70×10^{-9} mm^3/(N·mm) and then increased to 5.11×10^{-9} mm^3/(N·mm) as the test continued. In contrast, the wear rate of the P/M superalloy increased from 3.04×10^{-10} to 5.32×10^{-10} mm^3/(N·mm) before decreasing to 4.39×10^{-10} mm^3/(N·mm). These variations are attributed to the formation and evolution of high-hardness oxide composite wear debris on the contact surfaces, which is characteristic of typical three-body wear. Initially, ploughing by wear debris increases the wear rate. As friction progresses, debris accumulates and compacts into a high-hardness composite layer, which partially protects the surface and reduces the wear rate. Subsequent fracture of this debris layer generates additional ploughing, causing the wear rate to increase again.

(2) Under various working conditions, the COF gradually increases and then stabilizes over time. Lower normal loads lead to larger fluctuations in the COF, indicating that insufficient contact pressure cannot effectively compact the generated wear debris. This results in continuous surface ploughing during friction, destabilizing the surface and increasing the COF variability. As the normal load increases, the stable COF gradually decreases. Similarly, an increase in the sliding frequency also leads to a lower stable COF.

(3) According to calculations and comparisons with experimental data, the error between the friction coefficient predicted via Eq. (9) and the measured friction coefficient is within 20%. These findings indicate that the friction coefficient model can reliably predict the COF of P/M superalloy under different working conditions, enabling correction and improvement of the wear model for various operational scenarios.

(4) The wear model that accounts for variations in the friction coefficient demonstrates high accuracy in predicting wear under different cycles and load conditions, with wear depth errors within 5 μm. However, the simulation does not capture the observed reduction in the central height of the contact area as the load increases.

Acknowledgements

This work was supported by the Science Center for Gas Turbine Project (No. P2023-B-III-002–001), the National Natural Science Foundation of China (Nos. 52575182 and 91860111), the Research Fund of the State Key Laboratory of Mechanics and Control for Aerospace Structures (Nanjing University of Aeronautics and Astronautics) (No. MCAS-I-0325K01), and the National Key Laboratory of Marine Engine Science and Technology.

Declaration of competing interest

The authors have no competing interests to declare that are relevant to the content of this article.

References

[1] Archard J F. Contact and rubbing of flat surfaces. *J Appl Phys* **24**(8): 981–988 (1953)
[2] Fouvry S, Paulin C. An effective friction energy density approach to predict solid lubricant friction endurance: Application to fretting wear. *Wear* **319**(1–2): 211–226 (2014)
[3] Fouvry S, Kapsa P. An energy description of hard coating wear mechanisms. *Surf Coat Technol* **138**(2–3): 141–148 (2001)
[4] Mary C, Fouvry S. Numerical prediction of fretting contact durability using energy wear approach: Optimisation of finite-element model. *Wear* **263**(1–6): 444–450 (2007)
[5] Teng X X, Luo Z, Yu X, Chang J, Zhao J, Xu C Y. A wear simulation approach based on the energy consumption model and its application to the VSV bushing wear analysis. *Tribol Int* **195**: 109609 (2024)
[6] Mindlin R D, Deresiewicz H. Elastic spheres in contact under varying oblique forces. *J Appl Mech* **20**(3): 327–344 (1953)
[7] Woydt M, Mohrbacher H. Friction and wear of binder-less niobium carbide. *Wear* **306**(1–2): 126–130 (2013)
[8] Li L, Zhang W, Li G H, Wang J J, Li L X, Xie M X. Simulation study of thermal–mechanical coupling fretting wear of Ti-6Al-4V alloy. *Appl Sci* **12**(15): 7400 (2022)
[9] Jahangiri M, Hashempour M, Razavizadeh H, Rezaie H R. A new method to investigate the sliding wear behaviour of materials based on energy dissipation: W–25wt%Cu composite. *Wear* **274–275**: 175–182 (2012)
[10] Yue T Y, Abdel Wahab M. A numerical study on the effect of debris layer on fretting wear. *Materials* **9**(7): 597 (2016)
[11] Choudhry J, Almqvist A, Larsson R. Improving archard's wear model: An energy-based approach. *Tribol Lett* **72**(3): 93 (2024)
[12] Liskiewicz T, Fouvry S, Wendler B. Impact of variable loading conditions on fretting wear. *Surf Coat Technol* **163**: 465–471 (2003)
[13] Shen F, Hu W P, Meng Q C. A damage mechanics approach to fretting fatigue life prediction with consideration of elastic–plastic damage model and wear. *Tribol Int* **82**: 176–190 (2015)
[14] Zhang H B, Etsion I. An advanced efficient model for adhesive wear in elastic: Plastic spherical contact. *Friction* **10**(8): 1276–1284 (2022)

[15] Wang J, Chen T J, Zhou C Z. Crystal plasticity modeling of fretting fatigue behavior of an aluminum alloy. *Tribol Int* **156**: 106841 (2021)
[16] Yang Y L, Wang C L, Gesang Y, Shang H F, Wang R, Liang Y M, Wang T C, Chen Q, Shao T M. Fretting wear evolution of γ-TiAl alloy. *Tribol Int* **154**: 106721 (2021)
[17] Cheng J, Yang J, Zhang X H, Zhong H, Ma J Q, Li F, Fu L C, Bi Q L, Li J S, Liu W M. High temperature tribological behavior of a Ti-46Al-2Cr-2Nb intermetallics. *Intermetallics* **31**: 120–126 (2012)
[18] Liu D, Zhang L J, Mi L, Guo K, Xue X Y. Preparation and application status of TiAl alloy. *Titanium Ind Prog* **31**(4): 11–15 (2014) (in Chinese)
[19] Yang R. Advances and challenges of TiAl base alloys. *Acta Metall Sin* **51**(2): 129–147 (2015) (in Chinese)
[20] Huttunen-Saarivirta E, Kilpi L, Hakala T J, Metsäjoki J, Ronkainen H. Insights into the behaviour of tool steel-aluminium alloy tribopair at different temperatures. *Tribol Int* **119**: 567–584 (2018)
[21] Xu G, Chen B, Feng K, Zhang D Y, Zhu P X. Study on wear performance of GS-18NiMoCr36/42CrMo friction pair. *IOP Conf Ser: Mater Sci Eng* **772**(1): 012095 (2020)
[22] Dong C L, Yuan C Q, Li J, Li J, Yan X P. Study on tribological properties of Al_2O_3 ceramics/$1Cr_{18}Ni_9Ti$ stainless steel rubbing pairs in H_2O_2 solutions. *Lubr Sci* **23**(1): 41–48 (2011)
[23] Chen H H, Jiang T, Liu C K, Liu C J, Wang J N, Liu Y F. Friction and wear properties of friction pairs of DD6/GH3536 superalloy. *Fail Anal Prev* **15**(2): 84–90 (2020) (in Chinese)
[24] Zhao W, He W F, Liang X Q, Huang Z B, Zhou Q, Pang Z C, Song J D, Hu S, Cui L Q, Luo S H. Enhancing elevated-temperature fretting wear performance of GH4169 by tuning wear mechanism through laser shock peening. *Tribol Int* **192**: 109215 (2024)
[25] Wang S J, Yue T Y, Wang D G, Abdel Wahab M. Effect of wear debris on fretting fatigue crack initiation. *Friction* **10**(6): 927–943 (2022)
[26] Yang Y L, Gesang Y, Xu J M, Liang Y. Investigation on fretting wear of NiCrAlY coatings at elevated temperature. *Surf Coat Technol* **459**: 129339 (2023)
[27] Zhang C Z, Shen F, Ke L L. Electrical contact resistance endurance of AgNi10 alloy under fretting wear: Experiment and numerical prediction. *Wear* **530–531**: 205009 (2023)
[28] Jin F, Li J L, Liu P, Nan X J, Li X, Xiong J T, Zhang F S. Friction coefficient model and joint formation in rotary friction welding. *J Manuf Process* **46**: 286–297 (2019)
[29] Baydoun S, Fouvry S, Descartes S. Modeling contact size effect on fretting wear: A combined contact oxygenation—Third body approach. *Wear* **488–489**: 204168 (2022)
[30] Arnaud P, Fouvry S, Garcin S. A numerical simulation of fretting wear profile taking account of the evolution of third body layer. *Wear* **376–377**: 1475–1488 (2017)
[31] Yang Y L, Xu J M, Liang Y. A fretting wear model considering formation of tribolayers. *Ind Lubr Tribol* **75**(4): 372–379 (2023)
[32] Springis G, Boiko I. Comparative analysis of wear models for accurate wear predictions. *Lubricants* **13**(3): 100 (2025)
[33] Wang H, Zhang L J, Zhang W J, Li H T, Chi H, Yang K, Zhou J X, Ai L. Research on node-improved energy dissipation wear model for fretting fatigue prediction in railway press-fit shaft. *Wear* **574–575**: 206104 (2025)
[34] Maalekian M. Friction welding–critical assessment of literature. *Sci Technol Weld Join* **12**(8): 738–759 (2007)
[35] Zhang Y B, Lu L T, Zou L, Zeng D F, Zhang J W. Finite element simulation of the influence of fretting wear on fretting crack initiation in press-fitted shaft under rotating bending. *Wear* **400–401**: 177–183 (2018)
[36] Yue T Y, Abdel Wahab M. Finite element analysis of fretting wear under variable coefficient of friction and different contact regimes. *Tribol Int* **107**: 274–282 (2017)

Shaomeng Li graduated from Nanjing University of Aeronautics and Astronautics (NUAA) with his bachelor degree in aircraft power engineering in 2022. In 2025, he obtained his master degree from NUAA, China, under the supervision of Prof. Hongjian Zhang. His research focuses on fretting fatigue of joint structures and fretting fatigue resistance design.

Junqing Tan graduated from Nanjing University of Aeronautics and Astronautics with his bachelor degree in mechanical engineering in 2023. He is now a Ph.D. candidate of Nanjing University of Aeronautics and Astronautics, under the guidance of Prof. Hongjian Zhang. His research directions include fretting fatigue damage mechanism and fatigue life prediction of materials. His research focuses on the surface protection technology of materials.

Chao Wang received his bachelor degree in vehicle engineering from Beijing Institute of Technology in 2022. He is currently a master graduate student at Nanjing University of Aeronautics and Astronautics (NUAA), supervised by Prof. Hongjian Zhang. His research interests focus on elastoplastic contact mechanics, adhesive wear mechanisms, and mixed lubrication behavior, with a commitment to optimizing the tribological performance of mechanical systems.

Hongjian Zhang is now a professor and doctoral supervisor of Nanjing University of Aeronautics and Astronautics. In September 2009, he graduated from the aerospace propulsion theory and engineering major of Nanjing University of Aeronautics and Astronautics. He has been engaged in the scientific research work of aero-engine structure design, strength, fatigue, and optimization design for a long time. His main research fields include the damage mechanism and life assessment technology of advanced composite structures, fretting fatigue and life prediction of connecting structures.

Haitao Cui is now a professor and doctoral supervisor of Nanjing University of Aeronautics and Astronautics. He is mainly engaged in scientific research on the strength and fatigue of aero-engine structures. His main research fields include strength and life analysis of composite structures, fatigue and life prediction of high-temperature structures, fretting fatigue and life prediction of connecting structures, and structural reliability optimization design and topology analysis